



Electrocatalysis at palladium nanoparticles: Effect of the support nitrogen doping on the catalytic activation of carbon–halogen bond



Lorenzo Perini, Christian Durante, Marco Favaro, Stefano Agnoli, Gaetano Granozzi,
Armando Gennaro *

Department of Chemical Sciences, University of Padova, Via Marzolo, 1, 35131 Padova, Italy

ARTICLE INFO

Article history:

Received 20 May 2013

Received in revised form 2 July 2013

Accepted 8 July 2013

Available online 17 July 2013

Keywords:

Doped glassy carbon

Electrocatalysis

Palladium

Nitrogen doping

Benzyl chloride

ABSTRACT

Pd nanoparticles (NPs) were deposited electrochemically on three differently modified glassy carbon (GC) supports: pristine GC, nitrogen implanted GC and Ar implanted GC. The aim of such an approach is to discriminate whether the electrocatalytic activity of Pd NPs toward the activation of carbon–halogen bond is preferentially driven by chemical or morphological defects. Modified GC electrodes were prepared by ion implantation whereas Pd was deposited according to a double-step potential deposition in a 1 mM $\text{PdSO}_4 + 0.1 \text{ M H}_2\text{SO}_4$ solution.

The electrodes were fully characterized by X-ray photoemission spectroscopy, which allowed the identification of several different N-based defects. Pd NPs morphology, dimension and distribution were investigated by scanning electron microscopy. The outcomes indicate that the electrodeposition of Pd NPs on nitrogen-implanted GC results in smaller catalyst particle sizes and higher particle dispersion with respect to pristine GC. The palladium nitrogen-implanted electrode was tested in the electrochemical reduction of benzyl chloride, showing that Pd NPs result in a much higher catalytic activity than bulk Pd and Pd NPs loaded on the pristine GC electrode.

© 2013 Elsevier B.V. All rights reserved.

1. Introduction

Activation of the carbon–halogen (C–X) bond is a highly explored field in organic electrochemistry since it finds huge application in organic synthesis [1,2], in the control over radical polymerization [3,4], in pollutant degradation [5–7] and in mechanistic investigation on dissociative electron transfer (DET) [8–11]. The main drawback associated with the electrochemical activation of C–X is the very negative potentials required, and this is particularly true in the case of organic chlorides, which represent the most investigated ensemble among organic molecules containing a nucleofuge group. This has boosted over the last decade the research of electrode materials active toward the C–X bond breaking, and, so far, Ag, Cu and Pd were found to possess extraordinary electrocatalytic properties [12–16]. However, attempts to improve catalytic activity by changing from bulk electrode to nanoparticles (NPs) dispersed on a support, or by introducing a second or a third metal have not yet led to the desired improvements [17,18].

In principle, the catalytic activity can be increased either by a fine dispersion of the NPs or by modulating the electronic properties of the catalyst NPs by interaction with support chemical

or morphological defects; as an example, a way to enhance the durability of the catalyst support assembly in the case of oxygen reduction is to strengthen the catalyst NPs support interaction by introducing into the substrate defects that can act as trapping sites for anchoring the catalyst NPs [19,20]. In this regard, Minguzzi et al. have recently observed that the electrochemical activation of a carbon surface in acidic media introduces oxygen functional groups which enhances the stability and the electrocatalytic activity of Ag NPs toward the C–X bond activation [21].

Among various forms of carbon, glassy carbon (GC) is the most important for use as an electrode in electrochemistry, since it shows very low electrical resistivity, it is non-porous and impermeable to gases, it has high chemical resistance and the widest potential range observed for graphitic carbon electrodes and, last but not least, it can be easily polished and managed [22]. This renders GC an optimal material for a basic investigation on how the chemical modifications of the support can affect the activity of the loaded catalyst. The chemical modification (hereafter referred to as doping) of a GC surface is generally performed by the adsorption or by the covalent bonding (grafting) of molecular catalyst or electronic mediators. Another option is to synthesize a doped GC by thermolysis of suitable carbon precursors (usually polymers) containing the desired heteroatoms [22,23] or by the mixture of resins and an inorganic source of heteroatoms, such as boric acid and ammonia [24]. In the present case, following a different approach, nitrogen

* Corresponding author. Tel.: +39 049 8275132; fax: +39 049 8275829.

E-mail address: armando.gennaro@unipd.it (A. Gennaro).

functional groups have been introduced on a GC support by N₂⁺ and N⁺ ion implantation, producing a modified N-GC support. Here it will be shown that the presence of nitrogen functional groups on the carbonaceous support can influence the nucleation and growth of metal NPs and promote their catalytic activity toward activation of the C–X bond.

In the present case, palladium was employed as metal NPs because of its excellent hydrogenation ability, which makes it an excellent catalyst in the electrochemical dechlorination of organic chlorides in aqueous media or organic–aqueous mixture [25–27]. The Pd NPs electrochemical deposition on N-GC (Pd@N-GC) has been carried out in a 1 mM PdSO₄ + 0.1 M H₂SO₄ solution by a double-step potential deposition.

The N₂⁺ and N⁺ ion implantation, besides the introduction of new functional groups, leads to the formation of an increased number of morphological defects; this opens a new issue about the possibility of disentangling the effects connected to the presence of new functional groups from those deriving from the morphological defects introduced by ion implantation. In order to discriminate between the two effects, we have performed the deposition of Pd also on pristine GC (Pd@GC) and on an Ar⁺ implanted GC (Pd@Ar-GC) samples, and used them as an internal reference to gauge the results. In particular, Ar-implantation determines relevant morphological defects, consisting in a re-hybridization of carbon atoms from C_{sp}² to C_{sp}³, but cannot induce chemical defects [28].

The prepared GC electrodes were fully characterized by X-ray photoelectron spectroscopy (XPS) and scanning electron microscopy (SEM), and the electrochemical reactivity was tested for the reduction of benzyl chloride, which so far is considered as a standard test molecule for investigating carbon–halogen bond activation.

2. Experimental

2.1. Chemicals

CH₃CN, (WWR, HPLC grade) was distilled over CaH₂ under a N₂ atmosphere. Tetraethylammonium tetrafluoroborate (TEABF₄) (Fluka, >98%) was recrystallized twice from EtOH and dried in a vacuum oven at 70 °C. Benzyl chloride (Fluka, ≥99.5%) and PdSO₄ (Alfa Aesar, 99.95%) were high-purity reagents and were used without further purification. Deionized water used for the experiments was previously twice distilled from KMnO₄.

2.2. Preparation and characterization of Ar-GC and N-GC substrates

The N- and Ar-GC samples were prepared by using the ion beam produced by the ion gun (Thermo VG Scientific) under the same conditions: 2.2 × 10⁻⁶ mbar background of N₂ or Ar, a beam energy of 500 eV and exposure time of 10 min, with an incidence angle of the ion beam equal to 45° with respect to the sample surface (the ion current measured during this treatment was 2.0 μA and the total dose of implanted atoms was around 5 × 10¹⁶ ion cm⁻²). The nitrogen/argon dose was evaluated to be about 15 at%.

The XPS characterization of the samples was performed in a UHV chamber (base pressure <5 × 10⁻⁹ mbar), equipped with a double anode X-ray source (Omicron), a hemispherical electron analyzer (VG Scienta). All XPS measurements were performed at room temperature, using non-monochromatic Mg-Kα radiation ($\hbar\nu = 1253.6$ eV) and a pass energy of 50 eV and 20 eV for the survey and high-resolution spectra, respectively. The calibration of the binding energy (BE) scale was carried out using Au 4f as reference. The N 1s and C 1s peaks were deconvoluted into individual components (after Shirley background removal) using symmetrical Voigt

functions, whereas the Pd 3d photoemission peaks were deconvoluted into chemical-shifted components using Doniach–Sunjich shape functions. In both cases, the χ² minimization was ensured by the use of the nonlinear least-squares routines.

SEM investigations were performed with a dual-beam FEI Nova 600i instrument, with a semi-in-lens cold cathode field emission scanning electron microscope source.

2.3. Electrochemical instrumentation

Electrochemical measurements were carried out either by use of a computer-controlled Autolab PGSTAT30 potentiostat or an EG&G PARC Model 273/A potentiostat. The electrocatalytic activity of the nanostructured surfaces for benzyl chloride reduction was investigated by means of cyclic voltammetry (CV) and was carried out in a three-electrode cell with a GC, either modified or unmodified, or Pd disk as working electrode. The counter electrode and the reference electrode were a Pt wire and Ag|AgI|Bu₄NI (0.1 M) in CH₃CN, respectively. The latter was calibrated after each experiment against the ferrocenium/ferrocene couple. The potentials measured against the Ag|AgI|I⁻ reference electrode were converted to the SCE scale, to which all potentials in the paper are referred, by using E⁰_{Fe+/Fc} = 0.391 V vs. SCE in CH₃CN [12]. The working electrodes were built from a GC plate (Tokai GC-20) and 2-mm diameter Pd wire (Alfa Aesar, 99.999%) and were polished to a mirror finish with silicon carbide papers of decreasing grain size (Struers, grit: 500, 1000, 2400, 4000) followed by diamond paste (3-, 1-, 0.25-μm particle size). They were then cleaned in ethanol in an ultrasonic bath for about 5 min. In several cases a slight passivation of the Pd electrode, resulting in a poor reproducibility of the data, was observed during the electrocatalytic experiments. When this happened, the electrode was activated by CVs until cathodic discharge.

The Pd NPs on GC, Ar-GC and N-GC were freshly prepared before each experiment by electrodeposition of Pd on an exposed area of 3-mm diameter GC disk. The GC samples (8 mm diameter) were either clamped in a Kel-F mask or enveloped in Teflon tape. The electrochemical deposition of Pd NPs was carried out in a three-electrode cell containing 1 mM PdSO₄ solution in 0.1 M H₂SO₄. GC, Ar-GC and N-GC disks were set as working electrode, while the counter electrode and the reference electrode were a Pt wire and a Hg|Hg₂SO₄|K₂SO₄ saturated electrode, respectively. The reference electrode was separated from the working electrode compartment through a salt bridge which avoided any contamination of the working electrode. The conversion of the potential measured vs. Hg|Hg₂SO₄|SO₄²⁻ to the SCE scale is obtained by addition of +0.373 V to the measured value. All experiments were carried out at 25 °C.

3. Results and discussion

3.1. Preparation of Pd nanoparticles (NPs) on pristine and doped GCs

We first investigated the redox reactions of palladium on GC by CV in 1 mM PdSO₄ + 0.1 M H₂SO₄ solution. The first negative-going scan obtained under these conditions shows no well-defined cathodic peak for the reduction of Pd²⁺ to Pd(0). CV obtained starting at an initial potential of 0.3 V vs. SCE and scanning in the negative direction at variable negative potential limits indicate that Pd deposition starts at a potential more negative than -0.05 V vs. SCE, which coincides with the equilibrium potential. This was confirmed by the appearance of a PdO peak on the reverse scan and by XPS measurements revealing the presence of Pd over the GC surface. A similar experiment has been carried out at N-GC, though in

Table 1

Optimized deposition conditions for Pd NPs on various GC supports.

	E_r (V) ^{a,b}	t_r (s) ^c	E_{nu} (V) ^b	t_{nu} (s)	E_{grow} (V) ^b	t_{grow} (s)	Q (C) ^d
GC	0.3	10	-0.25	0.1	-0.077	50	2.74E-4
Ar-GC	0.3	10	-0.25	0.1	-0.077	50	2.75E-4
N-GC	0.3	10	-0.25	0.1	-0.127	50	2.78E-4

^a Resting potential.

^b Potentials are vs. SCE.

^c Resting time.

^d Values obtained from the mean of at least 5 different experiments.

In this case the deposition of Pd started at a more negative potential than at pure GC (-0.1 V vs. SCE). On the basis of these results, Pd NPs were deposited on GC by a potentiostatic double-step deposition method, since this method allows better control over the dimension and dispersion of metal NPs; the optimized deposition conditions are summarized in Table 1. The first step (nucleation) was set at a sufficiently negative potential ($E_{nu} = -0.25$ V vs. SCE) to allow the deposition process to be controlled only by diffusion and, as a consequence, instantaneous nucleation of Pd takes place. In the second step (growth) the potential was set at $E_{grow} = -0.077$ V vs. SCE for GC and Ar-GC and $E_{grow} = -0.127$ V vs. SCE for N-GC. At these potentials the process is kinetically controlled and the Pd NPs grow without further nucleation of new sites. The solution was oxygen-free and unstirred during the depositions. The deposition current was recorded and integrated in order to determine the total deposition charge (Table 1). The results indicate that a comparable amount of charge is consumed for all three samples and therefore the mass of Pd loaded over the three different GCs is fairly similar.

Pd NPs deposited on GC and modified GCs show the typical electrochemical behavior of palladium nanostructured electrode (Fig. 1) [29,30], which is characterized by a hydrogen adsorption peak labeled as 1c and a hydrogen desorption peak 1a, a zone labeled as **a** where hydrogen evolution occurs and a zone **b** due to the oxidation of hydrogen atoms adsorbed during the negative-going scan onto the Pd(0) NPs, a zone **c** due to the formation of PdO and the zone **d** due to PdO reduction.

3.2. Morphological and chemical characterization of Pd NPs on pristine and doped GCs

We first investigated the different GCs surface chemistry by means of XPS: in Fig. 2a the survey spectra of the different samples after the electrochemical deposition of Pd (see Table 1) are shown. The surveys for all three samples clearly show similar features that account for the presence of Pd, carbon and oxygen, while nitrogen is present only in the case of Pd@N-GC. In this

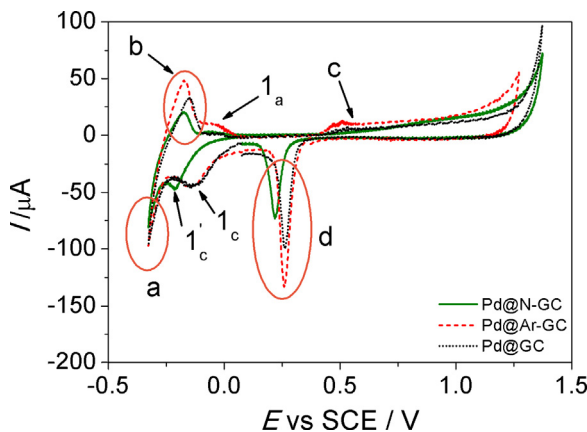


Fig. 1. Cyclic voltammetry of Pd NPs deposited on pristine and modified GCs in 0.1 M H_2SO_4 solution; scan rate 200 mV s⁻¹.

case, from the analysis of N 1s and C 1s XPS peaks, we can determine an overall surface stoichiometry of $C_{0.85}N_{0.15}$. Furthermore, while in Pd@Ar-GC we observe only morphological defects, consisting of a re-hybridization from C_{sp^2} to C_{sp^3} , in Pd@N-GC, we can distinguish between different chemical defects; by deconvoluting the N 1s XPS peak (Fig. 2b), we can single out the presence of pyridinic (398.0 eV), $-C\equiv N$ terminal groups (398.9 eV), pyrrolic (400.1 eV), N graphitic defects (401.2 eV) and N^+ ion trapped into carbon vacancies (402.6 eV) [28,31]. A further component present at high BE (404 eV) can be assigned to the interaction between nitrogen and oxygen with the formation, of NO_x groups, though in a very limited amount. Although GC has a randomly oriented structure over large dimensions, it contains a graphitic microcrystalline structure; therefore, we may assume that the effect of the ion implantation would increase the number of defects on the graphitic structures, resulting in an increased numbers of edges. If so, it is reasonable to assume that nitrogen groups are placed nearby these new edges of the graphitic microstructure. A pictorial view of nitrogen defects is proposed in Fig. 3.

Fig. 2c shows the Pd 3d XPS spectra for the same Pd loading (see Table 1) deposited onto Ar-GC, N-GC and GC. As can be seen, the Pd 3d photoemission peak presents a full width at half maximum (FWHM) compatible with the presence of both metal Pd and Pd^{2+}

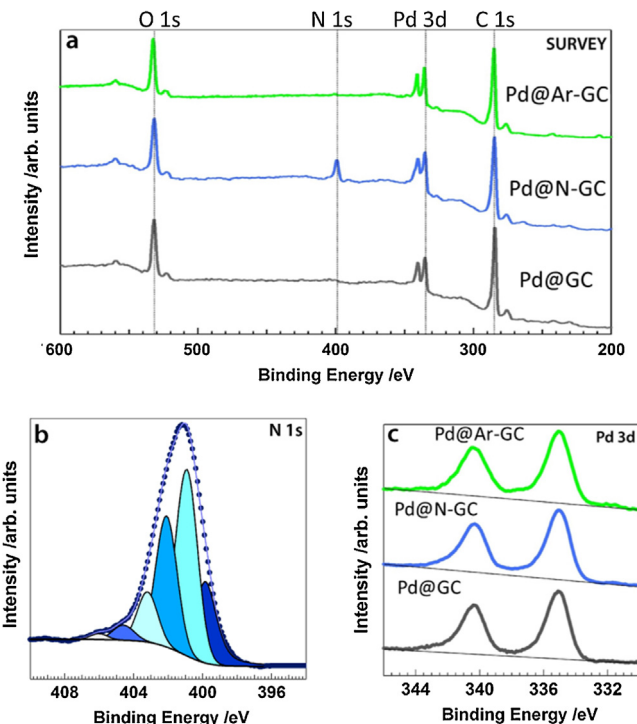


Fig. 2. XPS data of Pd@Ar-GC, Pd@N-GC, Pd@GC for the same Pd loading (see Table 1): (a) survey wide scans; (b) N 1s XPS peak and relative deconvolution by means of chemically shifted components in Pd@N-GC; and (c) Pd 3d XPS peaks.

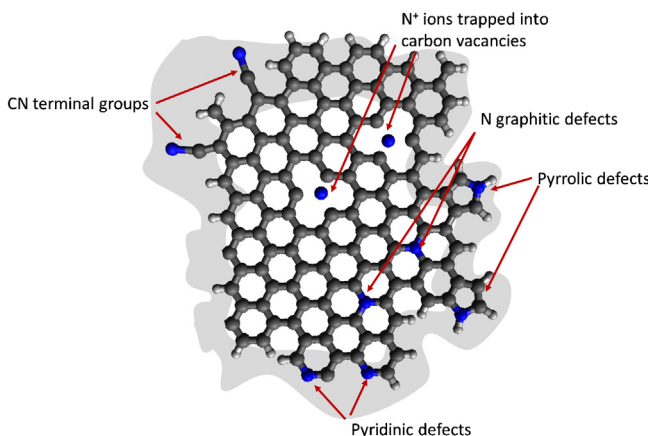


Fig. 3. Ball-and-stick model of the different chemical species obtained after ion implantation in GC according to the XPS N 1s data reported in Fig. 2b. The evidenced area corresponds to edge defects.

species (BE Pd⁰ = 335.1 eV, BE Pd²⁺ = 336.2 eV), and no significant change is observed in the three cases.

The morphological surface characterization of Pd NPs on doped and undoped GC supports was carried out by SEM (Figs. 4 and 5). The electrochemical deposition of Pd on GC has been carried out at three different deposition time: 25, 50 and 150 s, and results in the formation of NPs of an average dimension depending on the time of the growing step (t_{grow}). NPs deposited for 25 s have a typical Volmer–Weber growth and average dimension of 23 nm (Fig. 4a and b). The increase of the growing step period from 25 to 50 s increases the Pd amount loaded over the GC support and changes the Pd NPs dimensions according to a Gaussian distribution centered at 40 nm (Fig. 4c and d). It is worth noting that in this case NPs agglomerates of 100–300 nm sizes are also present as a result of the preferential growth of Pd NPs over the preexisting metal seeds. At a deposition time of 150 s the distribution of the particle

size assumes a maxima at 45 nm. In this case the growth of NPs agglomerates is even more emphasized (Fig. 4e and f).

In Fig. 5a comparative panel for Pd@GC, Pd@Ar-GC and Pd@N-GC deposited at the same growing period of 50 s, at two different magnification scale is reported. SEM images of Pd@Ar-GC show Pd NPs with smaller sizes (centered at 25 nm) and narrower dispersion (Fig. 5d–f) with respect to Pd@GC (Fig. 5a–c). Also in the case of Pd@Ar-GC some large size Pd agglomerates are visible, though to a lesser extent than for Pd@GC. In the case of Pd@N-GC, roughly spherical Pd NPs with average sizes of 21 nm are more regularly distributed with respect to both Pd@GC and Pd@Ar-GC (Fig. 5g–i).

The surface area of the Pd NPs loaded on pristine GC (geometric area 0.076 cm^2) and modified GCs have been estimated from the integrated charge in the electrochemical formation of a full monolayer of PdO [32,33]. This method is based on the identification of the upper potential limit at which oxygen is chemisorbed in a monoatomic layer with a one to one correspondence with the surface Pd atoms. This method has been preferred over the one based on CO stripping, since the N-GC support has shown an anomalous behavior in the presence of carbon monoxide.

CVs at variable positive potential limits have been performed (Fig. 6a) and then the integrated charge for the formation of PdO has been plotted vs. the inversion potential (Fig. 6b). The potential for a complete formation of a PdO monolayer corresponds to the point where the straight line changes its slope. The integrated charge at this potential allows obtaining the Pd NPs surface area according to Eq. (1):

$$Q_0 = 2eN_A \Gamma_0 A \quad (1)$$

where N_A is the Avogadro constant and Γ_0 is the surface concentration of atomic oxygen, which corresponds to the number of Pd atoms, N_{Pd} , exposed per unit surface area. From the N_{Pd} per unit surface area, it is possible to calculate the reference charge q_0^s , which in the case of Pd is ca. 420 C/cm^2 . The real surface area is therefore

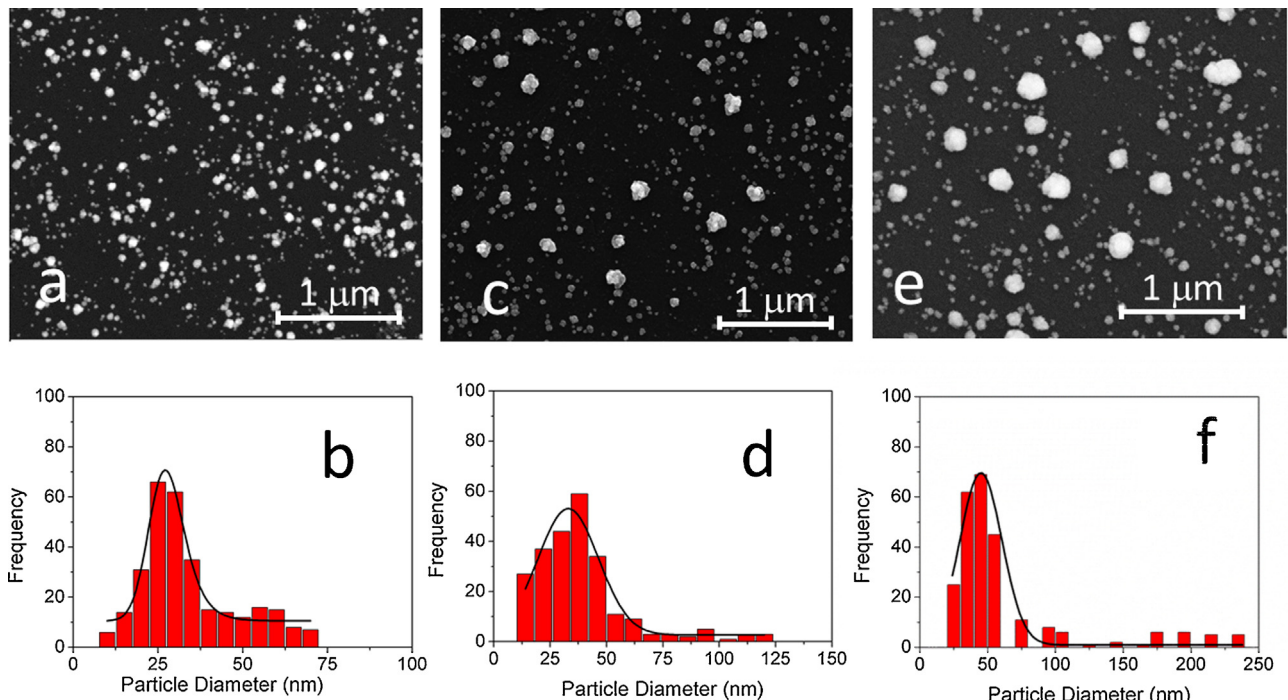


Fig. 4. SEM images and particle size distributions for Pd@GC at different growth time: (a and b) $t_{\text{grow}} = 25 \text{ s}$; (c and d) $t_{\text{grow}} = 50 \text{ s}$; (e and f) $t_{\text{grow}} = 150 \text{ s}$.

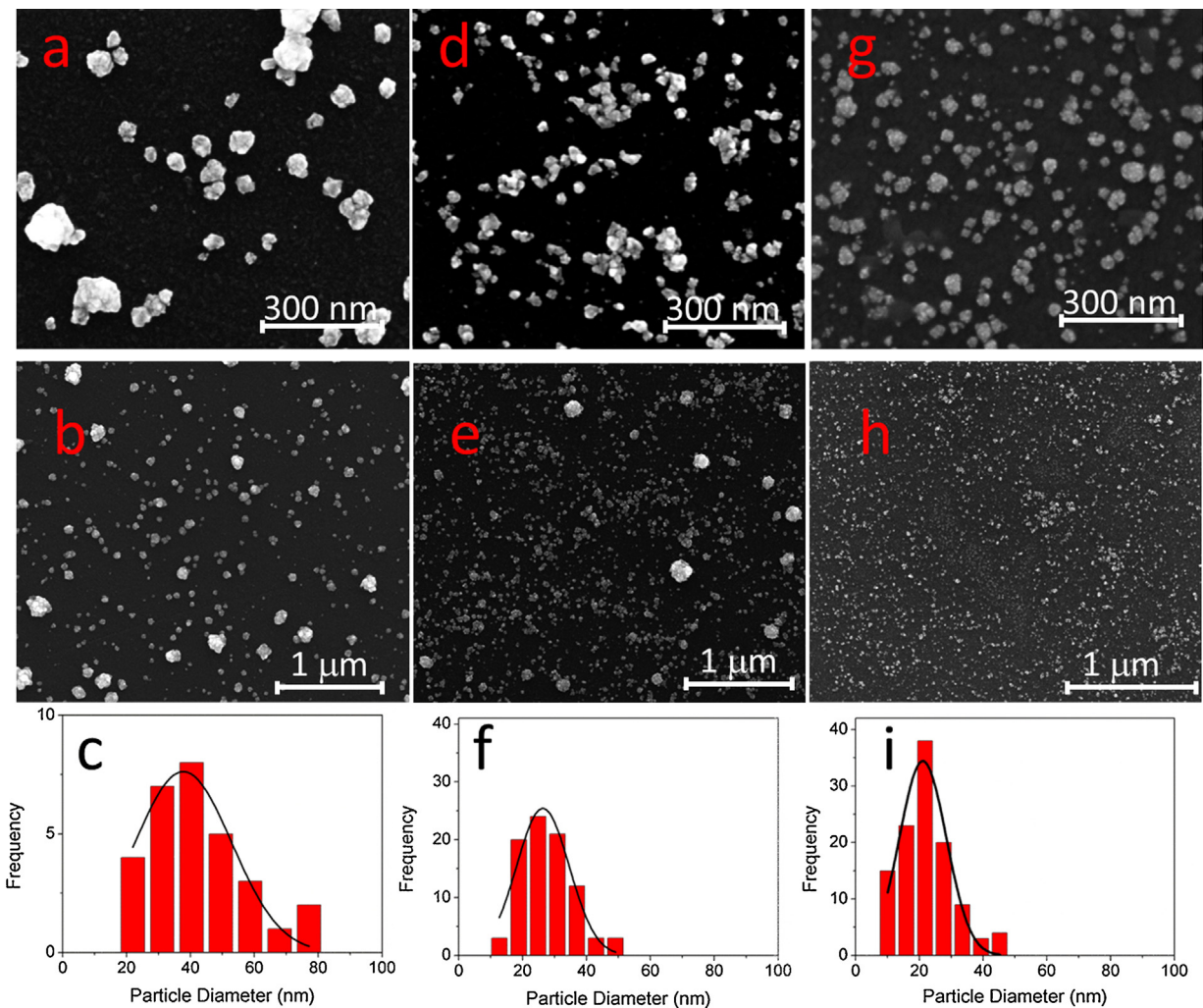


Fig. 5. SEM images at two different magnifications and particle size distributions for: (a–c) Pd@GC; (d–f) Pd@Ar-GC and (g–i) Pd@N-GC obtained at the same Pd loading (see Table 1).

obtained from the ratio of the integrated charge and the reference charge as indicated in Eq. (2):

$$A = \frac{Q_0}{q_0^s} \quad (2)$$

The estimated area for Pd@N-GC was 0.110 cm^2 , which is higher than the area calculated for Pd@GC and Pd@Ar-GC, 0.089 and 0.085 cm^2 , respectively.

In conclusion, it is evident that a mere morphological effect of the GC support is not sufficient to justify such differences in terms of surface area, metal NPs dimension and dispersion, but it must be related to the presence of nitrogen functional groups and a much stronger interaction between the chemical defect sites of GC and Pd [34]. A similar result has been observed for Pt NPs deposited on N-doped HOPG [35,36], where it was claimed the N-doping is responsible for a decrease in Pt NPs size and an increase in NPs dispersion.

3.3. Electrocatalytic activity of Pd NPs on pristine and doped GCs

The electrocatalytic activity of Pd NPs was tested for the reduction of benzyl chloride, chosen as a model process for the electroreduction of organic halides. The mechanism of activation of organic halides is generally analyzed in the framework of dissociative electron transfer (DET) to C–X bonds. Whether the activation

occurs at an inert or catalytic electrode, two reaction pathways are possible for the reductive cleavage of R–X to R[•] and X[−]. These are a stepwise mechanism, involving an intermediate radical anion, R–X^{•−}, which further decomposes to R[•] and X[−] (Eqs. (3) and (4)) and a concerted mechanism, where electron transfer (ET) and bond breaking occur in a single step (Eq. (5)). Whichever of the two mechanism is followed, a R[•] radical is formed that is generally more easily reducible than R–X and readily undergoes a second ET (Eq. (6)). Therefore, the process involves two successive one-electron transfers leading to the carbanion R[−], which is then rapidly protonated by any proton donor BH present in solution (Eq. (7)).



The transfer coefficient α , which allows the attribution of the reduction mechanism, has been determined by voltammetric analysis. If the peak potential E_p varies linearly with $\log v$, with slope $\partial E_p / \partial \log v$, Eq. (8) can be used to calculate the transfer coefficient,

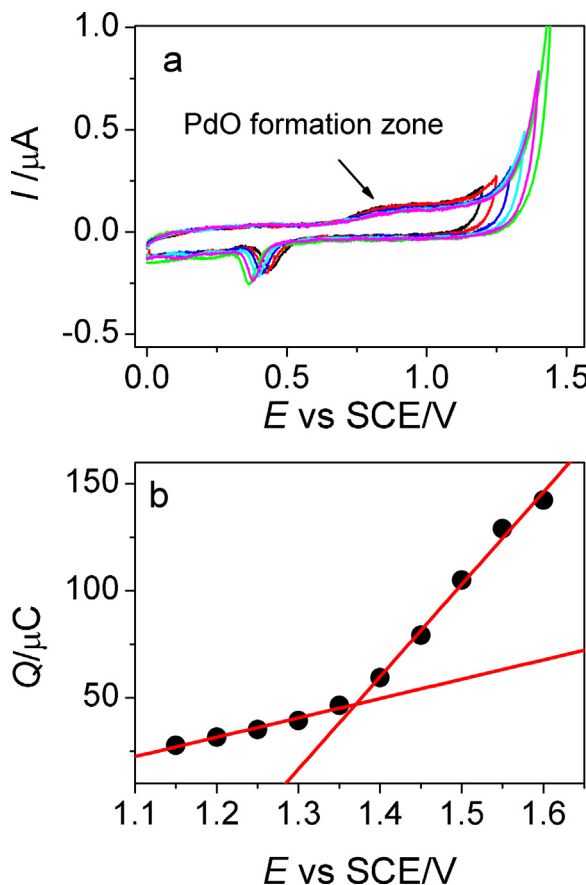


Fig. 6. (a) Cyclic voltammograms at Pd@N-GC electrode in 0.1 M H_2SO_4 with different positive potential limits. (b) Integrated charge for the formation of PdO at Pd@N-GC electrode as a function of the positive potential limit.

α. Alternatively, α can be calculated by Eq. (9), where $E_{p/2} - E_p$ is the peak width [37].

$$\frac{\partial E_p}{\partial \log v} = -\frac{1.151RT}{\alpha F} \quad (8)$$

$$E_{p/2} - E_p = \frac{1.857RT}{\alpha F} \quad (9)$$

The reduction mechanism of benzyl chloride on bulk Pd and GC has previously been reported [12], showing that, on both electrodes, the reduction of benzyl chloride follows a concerted mechanism that is typically characterized by an ET coefficient $\alpha \ll 0.5$.

The CVs of benzyl chloride on GC and bulk Pd in $\text{CH}_3\text{CN} + \text{TBABF}_4$ are reported in Fig. 7. Generally, the peak potential is the benchmark for the electrocatalytic properties, and GC is so far considered a

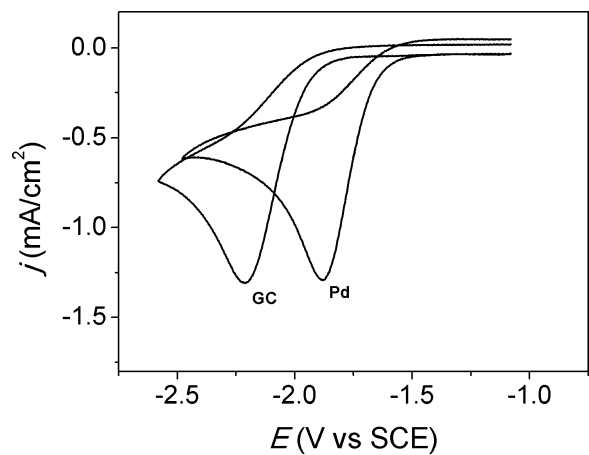


Fig. 7. Cyclic voltammetry of 2 mM benzyl chloride recorded in $\text{CH}_3\text{CN} + 0.1 \text{ M TBABF}_4$ at GC and bulk Pd electrodes.

non-catalytic electrode [38]. Therefore, the catalytic activity, expressed as $\Delta E_p = E_p^{\text{Pd}} - E_p^{\text{GC}}$, indicates that bulk Pd exhibits a remarkable electrocatalytic effect of 0.33 V with respect to GC (Table 2).

Fig. 8a shows CV of benzyl chloride reduction at Pd@GC electrodes at different Pd deposition times. From Fig. 8a it is clear that the overpotential for benzyl chloride reduction depends on the Pd surface coverage since, as the deposition time of Pd increases from 25 to 150 s, the reduction peak shifts to a more positive potential and the peak current increases. The best performance is observed at Pd@GC deposited for 150 s ($E_p = -1.87 \text{ V vs. SCE}$), which shows comparable electrocatalytic activity with respect to bulk Pd ($E_p = -1.88 \text{ V vs. SCE}$). Therefore, it appears that the catalytic activity of Pd over a non-modified GC depends more on the Pd loading and nanoparticles size than on the morphology of the metal catalyst.

The electrochemical behavior of Pd@Ar-GC ($t_{\text{grow}} = 50 \text{ s}$) is also reported in Fig. 8b. As previously discussed, Pd NPs on Ar-GC are smaller and more uniformly dispersed than on pristine GC; however, besides a little difference of peak current, which may be associated with a different active surface area, Pd@Ar-GC shows similar catalytic activity and reduction mechanism with respect to Pd@GC (Table 2). These results assert that, even though Ar-GC has an increased number of defects with respect to pristine GC and the Pd NPs size is sensibly different between the two samples, the catalytic activity is not influenced by the morphology of the supports. Furthermore, it must be stressed that both Pd@GC and Pd@Ar-GC do not show better performance in terms of catalytic activity with respect to bulk Pd, and this, also considering the benefit of employing a small amount of catalyst, puts a limit on the practical advantage of using a nanostructured electrode with respect to a bulk one.

Table 2

Voltammetric data for benzyl chloride reduction (2 mM) in $\text{CH}_3\text{CN} + 0.1 \text{ M TEABF}_4$, measured at 0.1 V s^{-1} .

Cathode	E_p ^a (V)	α	ΔE_p ^b (V)	A (cm^2)	$M\text{-CA}$ ^c (mA g^{-1})	$S\text{-CA}$ ^d (mA cm^{-2})
GC	-2.21	0.30		0.071 ^e	–	–
Pd	-1.88	0.26	0.33	0.031 ^e	–	1.262
Pd@GC	-1.93	0.19	0.28	0.089 ^f	7.2E+05	1.217
Pd@Ar-GC	-1.93	0.23	0.28	0.085 ^f	6.6E+05	1.156
Pd@N-GC	-1.78	0.33	0.43	0.110 ^f	9.0E+05	1.269

^a Potentials are referred to SCE.

^b See $\Delta E_p = E_p^{\text{Pd}} - E_p^{\text{GC}}$.

^c Mass catalytic activity with respect to the mass of Pd electrodeposited.

^d Specific catalytic activity.

^e Geometric area.

^f Real surface area.

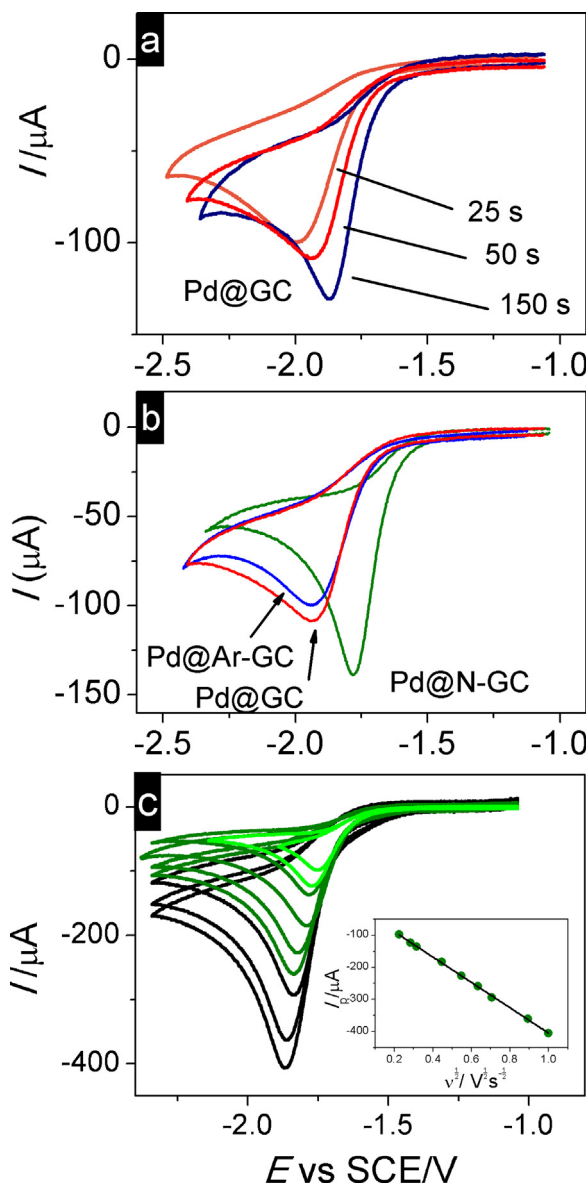


Fig. 8. Cyclic voltammetry of 2 mM benzyl chloride recorded in $\text{CH}_3\text{CN} + 0.1 \text{ M TBABF}_4$ at different electrodes: (a) Pd@GC at different Pd loading; (b) Pd@N-GC, Pd@Ar-GC and Pd@GC; and (c) effect of the scan rate at Pd@N-GC.

The electrochemical behavior was tested also at Pd@N-GC ($t_{\text{grow}} = 50 \text{ s}$) (Fig. 8b), and, this time, Pd@N-GC is more active in terms of overpotential, mass catalytic activity (peak current/grams of Pd) and specific catalytic activity (peak current/surface area) not only with respect to Pd@GC or Pd@Ar-GC, but also to bulk Pd (Table 2). The integrated current for the deposition process indicates that the Pd amount loaded on N-GC is comparable to that at Ar-GC; thus, the improved catalytic activity is not the result of different Pd loading or particle size on the three supports. This represents a clear example where the electroactive support exerts a synergistic action, promoting the catalytic activity of metal NPs toward a catalytic process. The nature of this increased catalytic activity derives from the interaction between nitrogen functional groups and Pd NPs during the reduction process since the Pd free N-GC was found to be not active by itself. Actually, both N-GC and Ar-GC supports result to be even less active than pristine GC by several mV. To verify that the increased catalytic activity is not the result of a different reduction mechanism, we have evaluated the dependence of the voltammetric peak from the scan rate (Fig. 8c).

The linear dependence of I_p from the square root of the scan rate indicates a diffusion-controlled process, while values of $\alpha = 0.33$ assert a concerted reduction mechanism, as already observed at Pd@GC and bulk Pd. Furthermore, Pd@N-GC is active even after several days at open atmosphere, indicating an intrinsic chemical and mechanical stability. This was confirmed also by *post eventum* XPS measurements that assert the same content of Pd and N.

Compared with other catalysts reported in the literature well-known to possess high catalytic activity, such as Ag, Pd@N-GC shows comparable catalytic activity with respect to bulk Ag, that so far is considered the best catalyst for R–X activation in non-aqueous solution [12], while it is far more active (several hundred mV) than Ag NPs of similar size (20–30 nm) deposited on GC [39].

4. Conclusions

Morphologically and chemically stable Pd NPs deposited on N-GC have been prepared by a double potential-step deposition in $\text{H}_2\text{O} + 0.1 \text{ M H}_2\text{SO}_4$ containing millimolar amounts of PdSO_4 . The NPs are spherical in shape with average dimension of 20 nm and are uniformly distributed over the N-GC surface. The presence of nitrogen functional groups introduced into GC support seems to influence the nucleation and growth kinetics during Pd NPs deposition, which results in smaller catalyst particle sizes and higher particle dispersion. The most striking result is that the presence of nitrogen functionalities promotes the catalytic performance of Pd NPs toward activation of the C–Cl bond, so extensively that Pd@N-GC is more active not only than Pd NPs loaded on undoped GC, but even than bulk Pd.

Acknowledgments

The research leading to these results has received funding from the European Union's Seventh Framework Programme (FP7/2007–2012) for Fuel Cell and Hydrogen Joint Technology Initiative under grant agreement no. [303492] 10. MF thanks Fondazione Cariparo for a PhD fellowship. We acknowledge financial support from Ateneo Italo-Tedesco/Deutsch-Italienisches Hochschulzentrum within the Vigoni bilateral framework.

References

- [1] A.A. Isse, C. Durante, A. Gennaro, *Electrochemistry Communications* 13 (2011) 810–813.
- [2] V. Joukov, J. Simonet, *Electrochemistry Communications* 12 (2010) 781–783.
- [3] A.J.D. Magenau, N.C. Strandwitz, A. Gennaro, K. Matyjaszewski, *Science* 332 (2011) 81–84.
- [4] N. Bortolamei, A.A. Isse, A.J.D. Magenau, A. Gennaro, K. Matyjaszewski, *Angewandte Chemie International Edition* 50 (2011) 11391–11394.
- [5] A.A. Isse, B. Huang, C. Durante, A. Gennaro, *Applied Catalysis B: Environmental* 126 (2012) 347–354.
- [6] C. Durante, B. Huang, A.A. Isse, A. Gennaro, *Applied Catalysis B: Environmental* 126 (2012) 355–362.
- [7] B. Huang, A.A. Isse, C. Durante, C. Wei, A. Gennaro, *Electrochimica Acta* 70 (2012) 50–61.
- [8] A.A. Isse, A. Gennaro, C.Y. Lin, J.L. Hodgson, M.L. Coote, T. Gulashvili, *Journal of the American Chemical Society* 133 (2011) 6254–6264.
- [9] C. Costentin, M. Robert, J.-M. Savéant, *Journal of the American Chemical Society* 125 (2003) 10729–10739.
- [10] Y.F. Huang, D.Y. Wu, A. Wang, B. Ren, S. Rondinini, Z.Q. Tian, C. Amatore, *Journal of the American Chemical Society* 132 (2010) 17199–17210.
- [11] A. Wang, Y.F. Huang, U.K. Sur, D.Y. Wu, B. Ren, S. Rondinini, C. Amatore, Z.Q. Tian, *Journal of the American Chemical Society* 132 (2010) 9534–9536.
- [12] A.A. Isse, S. Gottardello, C. Durante, A. Gennaro, *Physical Chemistry Chemical Physics* 10 (2008) 2409–2416.
- [13] C. Durante, A.A. Isse, A. Gennaro, *Journal of Applied Electrochemistry* 43 (2013) 227–235.
- [14] P. Poizot, J. Simonet, *Electrochimica Acta* 56 (2010) 15–36.
- [15] V. Joukov, J. Simonet, *Electrochemistry Communications* 12 (2010) 331–334.
- [16] J. Simonet, *Electrochemistry Communications* 7 (2005) 74–80.
- [17] G. Zhang, Y. Kuang, J. Liu, Y. Cui, J. Chen, H. Zhou, *Electrochemistry Communications* 12 (2010) 1233–1236.

[18] C. An, Y. Kuang, C. Fu, F. Zeng, W. Wang, H. Zhou, *Electrochemistry Communications* 13 (2011) 1413–1416.

[19] S. Pylypenko, A. Queen, T.S. Olson, A. Dameron, K. O'Neill, K.C. Neyerlin, B. Pivar, H.N. Dinh, D.S. Ginley, T. Gennett, R. O'Hayre, *Journal of Physical Chemistry C* 115 (2011) 13667–13675.

[20] S. Pylypenko, A. Queen, T.S. Olson, A. Dameron, K. O'Neill, K.C. Neyerlin, B. Pivar, H.N. Dinh, G.S. Ginley, T. Gennett, R. O'Hayre, *Journal of Physical Chemistry C* 115 (2011) 13676–13684.

[21] A. Minguzzi, O. Lugaresi, G. Aricci, S. Rondinini, A. Vertova, *Electrochemistry Communications* 22 (2012) 25–28.

[22] N.L. Pocard, D.C. Alsmeyer, R.L. McCreery, T.X. Neenan, M.R. Callstrom, *Journal of Materials Chemistry* 2 (1992) 771–784.

[23] T.X. Neenan, M.R. Callstrom, B.J. Bachman, R.L. McCreery, D.C. Alsmeyer, *British Polymer Journal* 23 (1990) 171–177.

[24] A.A. Perić-Grujić, O.M. Nešković, M.V. Veljković, Z.V. Laušević, M.D. Laušević, *Bulletin of Materials Science* 30 (2007) 587–593.

[25] Y. Fang, S.R. Al-Abed, *Applied Catalysis B: Environmental* 80 (2008) 327–334.

[26] Z. Sun, X. Wei, X. Hu, K. Wang, H. Shen, *Colloids and Surfaces A: Physicochemical and Engineering Aspects* 414 (2012) 314–319.

[27] S. Chen, Z. Qin, X. Quan, Y. Zhang, H. Zhao, *Chinese Science Bulletin* 55 (2010) 358–364.

[28] M. Favaro, L. Perini, S. Agnoli, C. Durante, G. Granozzi, A. Gennaro, *Electrochimica Acta* 88 (2013) 477–487.

[29] V.C. Diculescu, A.M. Chiorcea-Paquin, O. Corduneanu, A.M. Oliveira-Brett, *Journal of Solid State Electrochemistry* 11 (2007) 887–898.

[30] S. Guerin, G.S. Attard, *Electrochemistry Communications* 3 (2001) 544–548.

[31] M. Favaro, L. Perini, S. Agnoli, C. Durante, A. Gennaro, G. Granozzi, *Physical Chemistry Chemical Physics* 15 (2013) 2923–2931.

[32] A.N. Correia, L.H. Mascara, S.A.S. Machado, L.A. Avaca, *Electrochimica Acta* 42 (1997) 493–495.

[33] L.L. Fang, Q. Tao, M.F. Li, L.W. Liao, D. Chen, Y.X. Chen, *Chinese Journal of Chemical Physics* 23 (2010) 543–548.

[34] Y. Zhou, R. Pasquarelli, T. Holme, J. Berry, D. Ginley, R. O'Hayre, *Journal of Materials Chemistry* 19 (2009) 7830–7838.

[35] Y. Zhou, T. Holme, J. Berry, T.R. Ohno, D. Ginley, R. O'Hayre, *Journal of Physical Chemistry C* 114 (2010) 506–515.

[36] Y. Zhou, K. Neyerlin, T.S. Olson, S. Pylypenko, J. Bult, H.N. Dinh, T. Gennett, Z. Shao, R. O'Hayre, *Energy & Environmental Science* 3 (2010) 1437–1446.

[37] A.J. Bard, L.R. Faulkner, *Electrochemical Methods*, 2nd ed., John Wiley & Sons, New York, 2001.

[38] A. Gennaro, A.A. Isse, C.L. Bianchi, P.R. Mussini, M. Rossi, *Electrochemistry Communications* 11 (2009) 1932–1935.

[39] A.A. Isse, S. Gottardello, C. Maccato, A. Gennaro, *Electrochemistry Communications* 8 (2006) 1707–1712.